Real-time Surface Slope Estimation by Homography Alignment for Spacecraft Safe Landing

Yang Cheng

Abstract—This paper offers a real-time approach for simultaneously determining spacecraft motion and multiple 3D planar surfaces for spacecraft safe landing. The approach contains three algorithms: a multiple homography alignment algorithm, which constructs homographies under unified epipolar geometry; a closed-form motion estimation algorithm; and a simple routine for surface slope estimation. This approach has three significant advantages: first, it works well for both a simple planar scene and more complex 3D world containing many smaller planar surfaces; second, it decomposes a very large optimization problem into much smaller sub-problems that are computationally less expensive. This computational advantage means that this approach can be exploited in real time robotic operations such as during time critical spacecraft landing. Finally, this approach is very reliable and accurate. The effectiveness of this approach is determined quantitatively through extensive simulations and qualitatively with actual images*

I. INTRODUCTION

For in situ space exploration, to be able to recover the local surface slope and avoid to land on a steep terrain is a critical capability for spacecraft safe landing [19][20][21]. In general, lander slope toleration is about 15 degrees [22][23][24], therefore any slope estimation methods must be able to measure the surface slope with precision of a few degrees regardless terrain types (Fig. 1) and trajectory. Because of its small mass, low power usage and matured technology, camera and associated vision algorithms, such as structure from motion (SFM), are very attractive options [24].
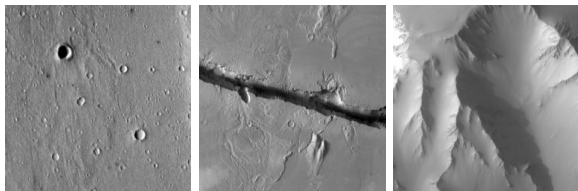

Figure 1: The potential landing site could be any of these places.

Since first being introduced by Ullman [1], SFM problem has received considerable attention, and a large number of algorithms have been suggested. These algorithms differ in the type of input (point, line or plane), the number of required images, and camera types (calibrated or uncalibrated, prospective or orthographic).

The problem of recovering the structure of a scene composed of point features from a pair or a set of images were first and the most extensively studied [1][2][3][4]. More sophisticated algorithms, such as incremental SFM based on the Extended Kalman Filter (EKF) [6][7], bundle adjustment [8] have been introduced later to improve accuracy and estimation stability.

A few researchers have considered the problem of reconstructing a scene composed entirely of straight lines segments. Taking advantage of their prominence in most man-made environment and the ease at which they can be extracted and tracked, researchers have reported good results using an objective function that minimizes reprojection error [9][10].

On the other hand, the SFM for plane surface has attracted some special attention because it presented some difficulty for these point based approaches [11][12][13][14][15]. Tsai and Huang suggested a solution of solving a sixth-order polynomial to determine the motion parameters [11]. Later they proposed a method of singular value decomposition (SVD) of the 3 by 3 homography matrix to recover the camera motion [12]. Longuet-Higgins presented a very elegant and simpler closed–form solution [14]. Weng & Huang have given a comprehensive analysis of the performance for plane surface reconstruction [15].

These planer surface motion algorithms work well only if the scene contains one dominating plane. When a scene contains multiple smaller planes, these algorithms become infeasible. Several attempts to overcome this problem have been suggested. For example, Luong suggested combining homography with the fundamental matrix for better motion estimation [16]. Irani et al suggested feature motion differencing between a homography and the rest of the scene to recover the motion [17]. This approaches works well when a large depth variation exists. But when the scene contains less depth variation, it does not work well. Bartoli et al [25] and Kirchhof [26] proposed to use fundamental matrix as consistency constrain in constructing multiple homographies which is a similar idea with this paper. But these algorithms are much more complicated than the approach proposed in this paper.

In addition, the methods for homography construction are problematic. Two standard methods are typically used in

Yang Cheng is with the Jet Propulsion Laboratory, Pasadena, CA USA (phone: 818-354-1856; fax: 818-393-5007; e-mail: ycheng@ jpl.nasa.gov).

constructing a homography—minimization of an image difference function [18] or using the point correspondence between two images to directly solve a set of linear equations [14][15]. However, because of image noise, computational error, or small patch size, the constructed homography is often error prone and as consequence large motion and reconstruction error are often observed.

Further more , because spacecraft descends at very high speed (> 30m/s) and the onboard computer is less powerful (less than one tenth of a regular desktop computer), a very fast SFM algorithm is needed for this time-critical operation.

II. BASIC MATHEMATICS

Consider a particular point $P=(X, Y, Z)$ on a plane surface in Cartesian coordinates relative to the first camera. The plane patch containing P can be represented as

$$N^T P = n_1 X + n_2 Y + n_3 Z = 1 \qquad (1)$$

where $N(n_1, n_2, n_3)$ is the normal vector of the plane surface. The distance d between the origin and the plane is $d = \|N\|^{-1}$

After some camera motion, the position of point P in the new camera frame is

$$P' = R(P - T) \qquad (2)$$

where R is a 3 by 3 rigid rotation matrix from the first camera frame to the second camera frame, T is the translation of the second camera in the first camera frame.

Combining (1) and (2), we obtain

$$P' = R(I - TN^T)P \qquad (3)$$

Let the images of P in the two camera frames have the coordinates

$$\begin{aligned} x = X/Z \quad y = Y/Z \quad z = 1 \\ x' = X'/Z' \quad y' = Y'/Z' \quad z' = 1 \end{aligned} \qquad (4)$$

Combining (3) and (4), we have a homography transformation between two images

$$x' = \frac{h_1 x + h_2 y + h_3}{h_7 x + h_8 y + 1} \quad y' = \frac{h_4 x + h_5 y + h_6}{h_7 x + h_8 y + 1} \qquad (5)$$

where $H = \begin{bmatrix} h_1 & h_2 & h_3 \\ h_4 & h_5 & h_6 \\ h_7 & h_8 & 1 \end{bmatrix} = sR(I - TN^T)$ and s is a scale factor.

Now assuming that H exists, the Longuet-Higgin algorithm will derive the vector T and N and the matrix R in a closed-form solution [14].

Consider a symmetric matrix W defined as

$$W = H^T H = (I - NT^T) R^T R (I - TN^T)$$

$$= (I - NT^T - TN^T + NN^T)$$

W can be diagonalized by an orthogonal matrix U:

$$UWU^T = Diag(d_1, d_2, d_3) \qquad (6)$$

Let $n = UN \quad t = UT \quad p = n - t$ then we have

$$\begin{bmatrix} 1 + p_1^2 - t_1^2 & p_1 p_2 - t_1 t_2 & p_1 p_3 - t_1 t_3 \\ p_2 p_1 - t_2 t_1 & 1 + p_2^2 - t_2^2 & p_2 p_3 - t_2 t_3 \\ p_3 p_1 - t_3 t_1 & p_3 p_2 - t_3 t_2 & 1 + p_3^2 - t_3^2 \end{bmatrix} = \begin{bmatrix} d_1 & 0 & 0 \\ 0 & d_2 & 0 \\ 0 & 0 & d_3 \end{bmatrix}$$

After some manipulations, four possible solutions are obtained as

$$t_1 = s_1 \sqrt{\frac{(d_1 - 1)d_3}{d_1 - d_3}} \qquad t_2 = 0 \quad t_3 = s_3 \sqrt{\frac{(1 - d_3)d_1}{d_1 - d_3}}$$

$$p_1 = -s_1 \sqrt{\frac{(d_1 - 1)d_1}{d_1 - d_3}} \qquad p_2 = 0 \quad p_3 = -s_3 \sqrt{\frac{(1 - d_3)d_3}{d_1 - d_3}} \quad (7)$$

$$n = t + p \qquad N = U^T n \quad T = U^T t$$

where $s_1 = \pm 1 \quad s_3 = \pm 1$

Among the four solutions, only two of them are visible (in front of camera), which is equivalent to the n_3 in N being greater than 0. Once the T and N are known, matrix R can be obtained as

$$R = \frac{H(I - TN^T)^{-1}}{\left\| H(I - TN^T)^{-1} \right\|} \qquad (8)$$

III. HOMOGRAPHY ALIGNMENT

In theory, a homography, which has 8 independent parameters, determines a camera motion (5 *dof*) and a plane surface normal vector (3 *dof*). If more than one plane (*m*) exists between two images, there will be total 8*m* parameters from *m* homographies to cover 5 + 3*m dof*, which is clearly an over determined system and is thus very sensitive to noise. If each homography is constructed independently, as mentioned before because of image noise, computational error, small size of interested area, these homographies often do not follow the same epipolar geometry. For example, nine homographies are independently constructed in a synthetic scene with image measurement error of 0.3 pixels (one sigma). In this case, the epipolar line is parallel to the x-axis. Any point in the first image can be projected to the second image by these homographies (Fig. 2a). If these homographies are free from any error, the projected points should align along a line (epipolar line). Unfortunately, these points do not lie along a line and this indicates inconsistence exists among these homographies. In this section, we offer a technique, homography alignment (HA), to unify all homographies into single epipolar geometry.
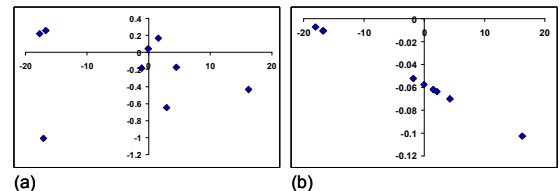

(a)　　　　(b)

Figure 2: (a). Inconsistence exits when homographies are constructed independently. (b). Homography alignment unifies all homographies into single epopolar geometry.

Suppose there are m plane patches in an image and their maps in the second images are represented as

$$H_1 = s_1 R(I - TN_1^T)$$
$$H_2 = s_2 R(I - TN_2^T)$$
$$....$$
$$H_m = s_m R(I - TN_m^T)$$ (9)

Now we have

$$\frac{s_1}{s_i} H_i - H_1 = s_1 RTN_1^T - s_1 RTN_i^T = K\Delta N_i^T$$ (10)

where
$$K = (k_1 \quad k_2 \quad k_3)^T = RT$$
$$\Delta N_i = (\Delta n_1 \quad \Delta n_2 \quad \Delta n_3)^T = s_1(N_1 - N_i)$$

Therefore, we have

$$d_i H_i = H_1 + K\Delta N_i^T \qquad i = 2,3,...m$$ (11)

H_1 is called the base homography and the relationships between the base homography and the rest of homographies is (11). The representation of equation (11) has several advantages. First, the total number of parameters has been reduced from original $8m$ to $5 + 3m$, which is exactly the degree of freedom of the system with m planar surfaces (eliminating the over determination problem). Second, this presentation is adaptive to the targeted scene's geometry. When the image scene is perfectly flat, the ΔN_i will degenerate to a null vector and all homographies will converge to single homography. Finally, this representation allows decomposing the homography constructions and motion estimation into two step processing.

First we assume H_1 and K are fixed, ΔN_i and H_i can be determined by a simple least-squares method on each individual patches. We define two vectors

$$V_1 = (k_1 x - k_3 xx' \quad k_1 y - k_3 yx' \quad k_1 - k_3 x')$$
$$V_2 = (k_2 x - k_3 xy' \quad k_2 y - k_3 yy' \quad k_2 - k_3 y')$$ (12)

Then we have

$$V_1 \Delta N_i = x'(h_7 x + h_8 y + 1) - (h_1 x + h_2 y + h_3) = b_{1i}$$
$$V_2 \Delta N_i = y'(h_7 x + h_8 y + 1) - (h_4 x + h_5 y + h_6) = b_{2i}$$ (13)

When n ($n>2$) correspondents in each patch are found, ΔN_i, which has three unknowns, can be determined by a least squares process.

On the other hand, when ΔN_i are fixed, the base homography H_1 and K can be updated globally by another linear least squares method.

We define three vectors

$$E_i = (x \quad y \quad 1 \quad 0 \quad 0 \quad 0 \quad -xx' \quad -yx' \quad \Delta N_i P \quad 0 \quad -x'\Delta N_i P)$$
$$F_i = (0 \quad 0 \quad 0 \quad x \quad y \quad 1 \quad -xy' \quad -yy' \quad 0 \quad \Delta N_i P \quad -y'\Delta N_i P)$$ (14)
$$G = (h_1 \quad h_2 \quad h_3 \quad h_4 \quad h_5 \quad h_6 \quad h_7 \quad h_8 \quad k_1 \quad k_2 \quad k_3)$$

where $\Delta NP = \Delta n_{i1} x + \Delta n_{i2} y + \Delta n_{i3}$

Then $\quad E_i G^T = x' \quad F_i G^T = y'$ (15)

We stack all correspondences from all plane patches together to form a linear system as,

$$MG^T = \begin{pmatrix} E_{11} \\ F_{11} \\ \vdots \\ E_{mn} \\ F_{mn} \end{pmatrix} G^T = \begin{pmatrix} x_{11}' \\ y_{11}' \\ \vdots \\ x_{mn}' \\ y_{mn}' \end{pmatrix} = B$$ (16)

The least squares solution gives an estimation of G as

$$\hat{G}^T = (M^T M)^{-1} M^T B$$ (17)

There are 11 unknowns in this system and the matrix computation is, therefore, quite fast.

Now we have this following homography alignment algorithm

1. Select a plane patch (largest in scene) as the base patch and construct its homography H_1.
2. Estimate the vector T_0, N_{10} and rotation matrix R_0 of this base patch by the Longuet-Higgins' algorithm described in last section and compute the $K_0 = R_0 T_0$.
3. Estimate ΔN_i for each individual patch using equation (13).
4. Estimate the global H_1 and K using equation (17).
5. Construct each individual homography using equation (11).
6. Compute the average reprejection error e, If e is smaller than a tolerance, go to step 7. Otherwise go to step 3.
7. Compute the vector T, N_1 and rotation matrix R of the base plane patch and compute the $K = RT$.
8. Update ΔN_i for each individual patch.

In general, it only takes a few iterations to converge. The purpose of step 7 and 8 is to unify the final homographies precisely into single epipolar geometry. As we know two sets of solutions can be obtained by the Longuet-Higgins algorithm. In most cases, the real solution can be picked out by checking the relationship between the camera pointing and the surface normal vectors. In practice, we run the HA procedure twice by using each set of solutions to initialize and pick up the solution with smaller reprojection error. Fig 2b. is the projected points after HA. Clearly they align along a single line.

Once the R, T, and N_1 are obtained, the rest of N_i can be easily calculated since $\Delta N_i = s_1(N_1 - N_i)$.

IV. EXPERIMENTAL RESULTS

This section describes a series of experiments that were carried out on both real images and simulated data in order

to evaluate the effectiveness of the proposed approach. First we define the three matrices that characterize the accuracy of the reconstructed plane patch and camera translation and rotation.

- Measuring camera motion error: We used the rotation error measurement suggested in [10]. Any rotation metric R can be written in the form $R = \exp\{\theta J(\overline{\omega})\}$ where $\theta \in [0, \pi], \hat{\omega}^T \hat{\omega} = 1$. The magnitude of a rotation is then defined as $\|R\| = \theta$. The rotation error is therefore defined as $\|\Delta R\| = \|\hat{R}^T R_t\|$ where $\hat{R}$ is the estimated rotation matrix and R_t is the ground truth rotation matrix. The translation error is defined as the angle between the unit vector of estimated translation and the true translation vector.

- Measuring structural error: Because we are interested in the surface slope, the structural error at here is defined as the angle between the estimated normal vector and the true normal vector.

4.1 SIMULATION EXPERIMENTS

A 60 degree field of view (FOV) with 1024 by 1024 pixels synthetic camera is used in this simulation. The purpose of this study is to determine the accuracy of the algorithms under different settings including the amount of error in image measurement and spacecraft trajectory. Three trajectories (0° vertical descending, 45° gliding and 90° horizontal fly) are used in this study (Fig. 3). The distance between the first camera and the second camera is one fifth of height above ground of the first camera. The imaged area is evenly divided into 3 by 3 grids and in each grid resides a plane patch. Total 40 sets of random terrain model (40 by 9 patches) are generated. 30 random points on each patch are created to simulate feature points and then they are projected to the first and second camera. The feature points in the second image are added Gaussian white noise with sigma from 0 to 1 pixel with 0.1 pixel increment. Total 1320 simulation trials were carried out.

Figure 4 shows how the accuracy of the camera motion as a function of the measurement error. As expected, the reconstruction error increases as measurement error increases. Among the three trajectories, the vertical descent one has the least accuracy. However, it is very interesting that the 45 degree gliding trajectory has the best accuracy. Under normal circumstance, in which the measurement error is less than 0.3 pixel one sigma, the rotation error for all three trajectories is less than 0.1 degree. The second figure is the translation error which has clear very strong correlation with the rotation error. Under the 0.3 pixel random measurement error assumption, the vertical descending trajectory has the largest error, which is roughly 0.5% of the true translation. For other two trajectories, the translation error is less than 0.25%. Suppose the maximum spacecraft horizontal velocity is 30m/s, the translation error of 0.25% is equivalent to ~8cm/s horizontal velocity error.

For a comparison with others, statistics of Longuet-Higgins motion was also obtained. We used average motions of nine independent motions by Longuet-Higgine method to calculate its statistics (dash lines in Fig 4). This study shows that the homography alignment method is at least two fold more accurate than the Longuet-Higgine method.
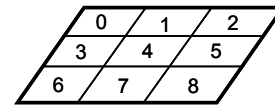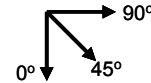

Figure 3: The simulated camera and surface configuration. The number in each grid is the window index.
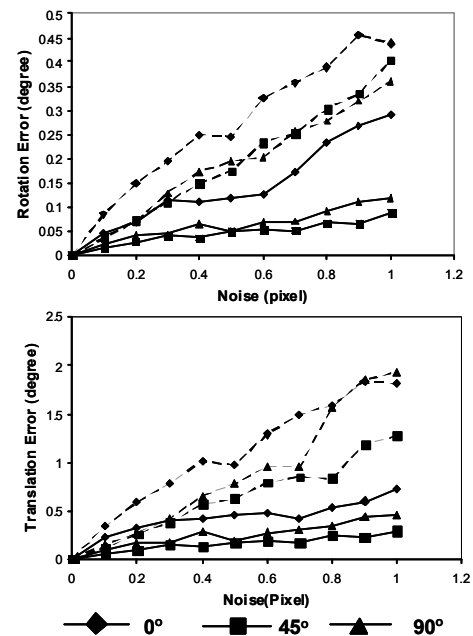

Figure 4: A comparison between the homography alignment and Longuet-Higgine method. Solid lines are from HA and dash lines are from Longuet-Higgine

Although there are 9 plane patches in this simulation, for the sake of saving space, we select window 3, 4, 5 as representatives of the best, the worst and average cases. Among these three windows, window 3 is farthest from the focal expansion and therefore the best case. The slope error is less than 0.5 degrees for all of these three trajectories if the measurement error is less than 0.3 pixels. The focal expansion is within the window 4 for the vertical descending, so it exhibits the worst slope accuracy. Window

5 represents roughly the average slope error of rest of windows. Under a normal circumstance, the slope error is less than 1°, which is well within the 15° slope tolerance of a lander[19][20][21].

In general, the proposed method only takes a few iterations to converge. Because the motion problem is decomposed into a base homography and a set of ΔN computations, the computation complexity is almost linear to the number of windows involved. Figure 6 shows its speed vs. the number of windows.
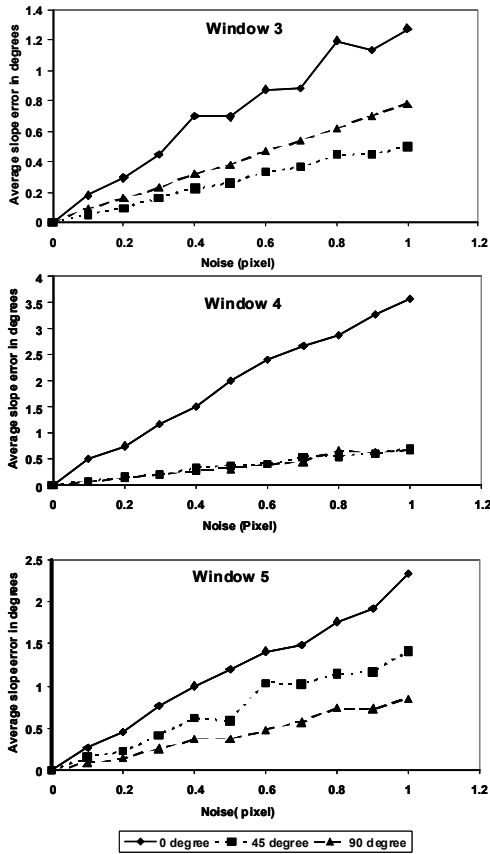

Figure 5: Average slope error as a function of the magnitude of the random errors in the point features. The top figure is for window 3, the middle figure is for window 4 and the bottom figure is for the window 5.
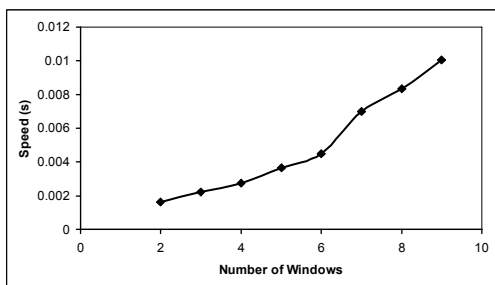

Figure 6: The average speed vs. the number of windows. The number of features in each window is 30 and this test was done on a Mac Pro with 2.8 GHz Intel Core processor.

4.2 REAL DATA EXPERIMENTS

Experiment 1: This experiment was carried out on the "descent" imagery collected at JPL Mars Yard. In order to validate the performance, a Point Grey Scorpion stereo image pair with 1 meter baseline was used in this data collection (Fig. 7). The camera FOV is 70 and 60 degrees horizontal and vertical respectively. The stereo pair is used to validate the performance. The first stereo image pair is about 13 meters above the ground and the second image pair is about 11 meters above the ground. We used the left images to emulate a descent image pair.

In the overlapped area between two descent images, nine 151 by 151 pixel windows, which are free from "craters" and "rocks", are selected (Fig. 7). In each patch, 60 point features are selected using the Forstner corner detection. They are matched in the second image using correlation method. In order to remove any outliers, we run RANSAC homography in each patch and all points surviving this procedure are then used in the motion estimation.

Figure 8 shows the 3D view of the spacecraft positions and nine recovered patches (red). The white point cloud under the each patch is from the stereo matching of upper stereo image pair. The gaps between recovered patches and point cloud are due the scale uncertainty of SMF. We fitted the point cloud under each patch to a plane and then calculated the angle of between these two normal vectors.
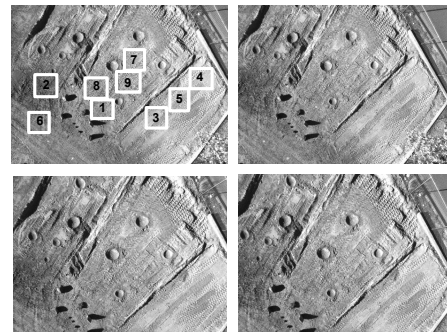

Figure 7: "Descent imagery" at JPL Mars Yard is used in this experiment. The top stereo pair is used to construct dense 3D model. The left pair is used in holography test. Nine patches (upper-left image) are selected as potential landing site candidates. The number in each box is the window index.
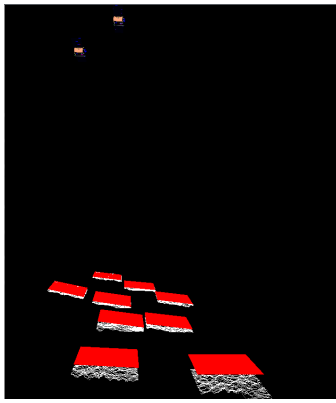
Figure 8: The 3D view of the spacecraft positions (upper left corner) and recovered surface patches (red). The white point cloud under each patch is from stereo matching of upper image pair.
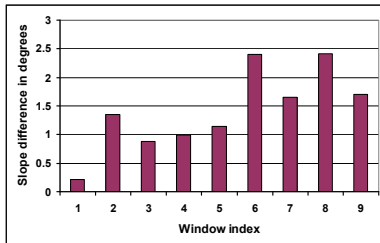

Figure 9: The slope difference between the proposed method and stereo matching.

Figure 9 shows the surface slope differences between this proposed method and stereo matching method. We can find that slope difference between two methods is within 3 degrees.

Experiment 2: Since urban scenes contain many planar surfaces, this proposed approach is suitable urban robotic operations. Figure 10 shows two "aerial" images over a manmade structure. Features in the first image are selected by using Forstner corner detection and then they are matched in the second image. We run RANSAC homography on the matched features and two planar patched are found (Fig 10). Then these two point sets are used in HA. Figure 11 shows the 3D point clouds of the two planes (left) and side of view of this structure (right). Visually, the reconstructed surfaces are consistent with the side view image.
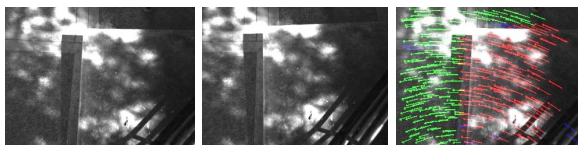

Figure 10: The "aerial" images over a manmade structure. The red arrows are features on the top of the platform and the green arrows are features on the ground**.**
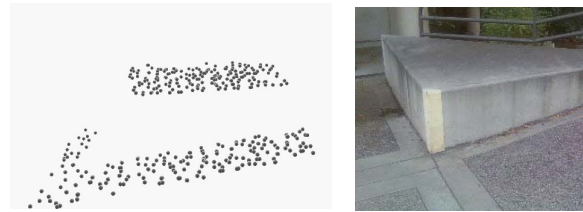

Figure 11: Left figure is the 3D view of the reconstructed 3D point clouds and right figure is a side view of this structure at similar view angle.

Experiment 3: For more complicated urban scenes, a simple feature RANSAC method may not work well. In this case, an image segmentation algorithm can be used in finding planer surfaces.

The procedure of the method is as following
1. Compute an image gradient magnitude image of the first image.
2. Threshold the gradient magnitude image and keep pixels with lower gradients and they are considered as interior of planer surfaces.
3. Run component labeling algorithm to obtain connected regions (Lower-left image of Fig. 12).
4. Pick the largest region and select and track features to the second image.
5. Construct a homography of the region using RANSAC.
6. Test the neighboring regions: If a neighboring region can be transferred to second image precisely, this neighboring will be merged to the mother region.
7. Execute step 4 to 6 for few times until no more regions can be merged any more (Lower–right image of Fig. 12)
8. Run homography alignment on the detected planer surfaces.
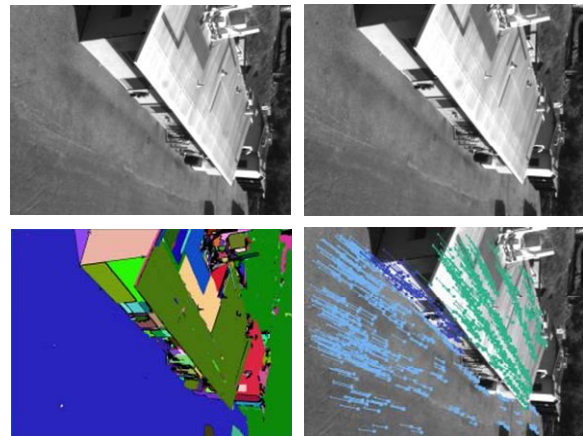9. Generate planer surfaces 3D models (Fig. 13).

Figure 12: An example of more complicated urban scene reconstruction. Top two images are motion pair. Lower-left image is a segmentation result of the first image. Lower-right image shows three dominating planes were found and features inside of them were tracked to second image.

Figure 13 shows multiple views of the reconstructed 3D model of the building and ground surfaces.
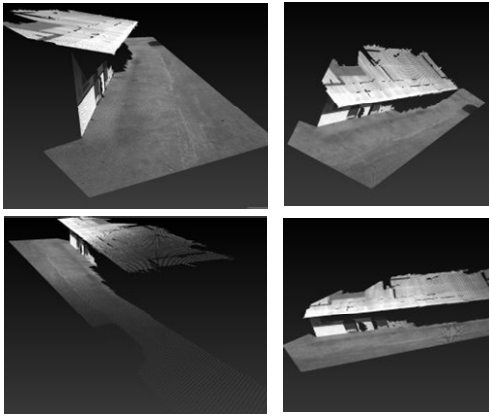
Figure 13: The 3D views of the reconstructed urban scene.

V. Conclusions

This paper presented a novel approach for recovering the surface structure and camera motion. The key idea is an ultra simple homography alignment algorithm that reduces the degrees of freedom from original $8m$ to $5+3m$ and makes the system very stable. After the HA, the motion estimation becomes a single plane motion estimation, which has a closed-form solution and the surface recovering becomes a simple linear manipulations.

Thousand of simulation experiments were carried out. All experiments produce valid results and no single test has failed, which indicates the system is very stable and reliable. The real data experiments show compatible result between the proposed method and stereo matching method. Under normal circumstances, the slope error is within a few degrees, which meets the future lander mission requirement.

In addition to space exploration, this approach is likely to perform well in places where many planar surfaces may be found, such as robotic navigation or 3D mapping indoors or in urban settings.

Further more HA can be extended to multiple image sequence motion estimation and structure modeling. In this case, a surface normal across multiple images is fixed, which will reduce the degrees of freedom even more.

Acknowledgments

References

[1] S. Ullman, The Interpretation of Visual Motion, The MIT Press, Cambridge, MA, 1979.

[2] Longuet-Higgine, H. C., "A computer algorithm for reconstructing a scene from two projections", Nature, London, 293, 133-135. 1981

[3] R. Hartley. "In defense of the 8-point algorithm," 5th Int'l Conf. on Computer Vision (ICCV'95), pp. 1064-1070, 1995

[4] J. Weng, T.S. Huang, and N. Ahuja, "Motion and structure from two perspective views: algorithms, error analysis and error estimation", IEEE Trans. PAMI, Vol. 11. no. 5 pp. 451-476, May 1989.

[5] Richard Hartley and Andrew Zisserman, "Multiple view geometry in computer vision", Cambridge University Press, second edition, 2003

[6] Oliver D. Faugeras, F. Lustaman, and G. Toscani, "Motion and structure from point and line matches", ICCV, 1987, pp. 25-33

[7] A. Chiuso, P. Favaro, H. Jin, and S. Soatto "3-D motion and structure causally integrated over time". ECCV, 2000.

[8] Manolis Lourakis and Antonis Argyros, "The design and implementation of a generic sparse bundle adjustment software package based on the Levenberg-Marquardt algorithm", FORTH-ICS/TR-340, 2004

[9] James L. Crowley et al, "Measurement and Interpolation of 3-D structure by tracking edge-line", International Journal of Compueter Vision, vol. 8. No. 1, pp. 29-52 July, 1992

[10] Camillo J. Taylor, David J. Kriegman "Structure and Motion from line segments in multiple images", IEEE Trans. On Pattern Analysis and Machine Intelligence, Vol. 17 No. 11, pp 1021-1033, November 1995

[11] R.Y. Tsai and T.S. Huang, "Estimatng three dimensional motion parameters of a rigid planar patch" IEEE Trans. Acoust. Speed, Signal Processing, Vo. ASSP-29, pp. 1147-1152, Dec. 1981.

[12] R. Y. Tsai, T. Huang, W. Zhu, "Estimating three dimensional motion parameters of a rigid planar patch,II: Singular value decomposition", IEEE Trans. Acoust. Speed, Signal Processing, Vol. ASSP-30, No. 4, Aug, 1982

[13] H. C. Longuet-Higgins, "The visual ambiguity of a moving plane", Proc. R. Soc. Lond. B. 223, 165-175 (1984).

[14] H. C. Longuet-Higgins, "The reconstruction of a plane from two perspective projection", Proc. R. Soc. Lond. B 227, 399-410, 1986.

[15] Juyamg Weng, N. Ahuja, T. Huang, "Motion and structure from point correspondences with error estimation: Plane surface", IEEE Trans. Signal processing, Vol. 39, NO. 12, Dec. 1991.

[16] Luong, Q.-T. and O.D. Faugeras, "Determining the fundamental matrix with planes: Instability and new algorithms"

[17] Michal Irani, B. Rousso, S. Peleg, "Recovering of Ego-Motion using region Alignment", IEEE PAMI, Vol. 19, No. 3, March, 1997

[18] R. Szeliski. Video mosaics for virtual environments. IEEE Computer Graphics and Applications, 16(2):22-30, March 1996

[19] Larry Matthies, Andres Huertas, Yang Cheng, Andrew Johnson " Landing Hazard detection with Stereo Vision and Shadow Analysis" AIAA infotech 2007

[20] D. Bernard and M. Golombek, "Crater and Rock Hazard Modeling For Mars Landing," AIAA Space Conference, Albuquerque, NM Aug. 2001.

[21] Y. Cheng, J Goguen, A. Johnson, C. Leger, L. Matthies, M. SanMartin and R. Willson, "The Mars Exploration Rovers Descent Image Motion Estimation System," IEEE Intelligent Systems 19 (3), 2004, 13-21

[22] Michael Watkins et al, "MSL Landing site selection: status of engineering capabilities and constrains and plan for site selection" 2nd MSL landing site selection workshop, Pasadena, CA 23-25, Oct 2007.

[23] Robert Braun and Robert Manning, " Mars exploration entry, descent and landing challenges" Aerospace Conference, 2006 IEEE.

[24] Larry Matthies et al "Stereo vision and shadow analysis for landing hazard detection" ICRA 2008, May 19-23

[25] Adrien Bartoli, Peter Sturm, Radu Horaud, "Projective Structure and Motion from Two Views of a Piecewise Planar Scene," ICCV, vol. 1, pp.593, Eighth International Conference on Computer Vision (ICCV'01) - Volume 1, 2001.

[26] Michael Kirchhof, "Linear constraints in two-view multiple homography estimation of uncalibrated Scenes", The International Archives of the Photogrammetry, Remote Sensing and Spatial Information Sciences. Vol. XXXVII. Part B3a. Beijing 2008.